Appl Phys B (2011) 104:989–1000
DOI 10.1007/s00340-011-4665-2

Applied Physics B
Lasers and Optics

Spectroscopy of CH_4 with a difference-frequency generation laser at 3.3 micron for atmospheric applications

M. Ghysels · L. Gomez · J. Cousin · N. Amarouche · H. Jost · G. Durry

Received: 8 November 2010 / Revised version: 8 June 2011 / Published online: 30 July 2011

Abstract The 3.25 micron spectral region is very suitable for the in situ sensing of CH_4 in the troposphere and the lower stratosphere with light-weight laser sensors. Several transitions of the strong fundamental ν_3 band of CH_4 are revisited in this spectral region using an ultra-compact Difference-Frequency Generation (DFG) laser. Accurate intensities as well as self-broadening coefficients are reported for several manifolds that are particularly relevant to the monitoring of CH_4. The study is extended to over hundred transitions reachable over the tunability range of the laser. Moreover, this DFG laser is the light source of a new, highly-compact CH_4 laser spectrometer to be operated from weather balloon. The CH_4 laser sensor is described and preliminary flight results are reported.

M. Ghysels (✉) · L. Gomez · J. Cousin · G. Durry
Groupe de Spectrométrie Moléculaire et Atmosphérique,
URM CNRS 6089, UFR Sciences Exactes et Naturelles,
Moulin de la Housse, BP 1039, 51687 Reims Cedex 2, France
e-mail: melanie.ghysels@univ-reims.fr
Fax: +33-(0)3-26913147

G. Durry
IPSL, Laboratoire Atmosphères, Milieux, Observations Spatiales,
UMR CNRS 8190, 78280 Guyancourt, France

N. Amarouche
Division Technique, l'Institut National des Sciences de l'Univers,
92195, Meudon Cédex, France

H. Jost
NovaWave Technologies, Inc., 900 Island Dr., Redwood City,
CA 94065, USA

1 Introduction

Methane is a greenhouse gas of major importance for the radiative balance of the Earth climate [1]. The methane concentration has dramatically increased by about 150% since the beginning of the industrialization era [2]. Main sources of CH_4 are wetlands, rice paddies, anthropogenic activity as fossil fuels and ruminant animals, and biomass burning [3]. Moreover, additional methane sources due to global warming may be another threat to climate: melting permafrost may cause large methane emissions into the atmosphere [4]. In this context, the global monitoring of methane is of high importance. Purposely, we have started, with the help of the French space agency (CNES) and of the CNRS, the development of a compact CH_4 sensor to be operated from weather balloons and based on the Difference Frequency Generation (DFG) laser technology. Such laser sensors launched from a network of meteorological stations could be an excellent complement to satellite observations to achieve a global mapping of CH_4 sources and sinks. Furthermore, methane may be used as a tracer of air masses in the upper troposphere and the lower stratosphere to investigate the impact of deep convection (in the tropical regions) and of isentropic transport on stratospheric H_2O [5]. Methane is also a source of H_2O in the stratosphere (by oxidation). Therefore, this new CH_4 sensor may also be very useful to address the study of the H_2O budget in the stratosphere which is a very important issue due to the potential impact of H_2O on the radiative balance of the stratosphere and consequently on the ozone layer [6–8].

To meet these science objectives, the laser sensor weight should be of less than 5 kg for the overall gondola; the in situ CH_4 concentration are to be measured continuously in the troposphere and the lower stratosphere at a temporal resolution of less than 1 s and with a precision of less than 5%.

Table 1 Comparison between predicted absorption depth for the SDLA spectrometer [21] ($L = 56$ m) and the PicoSDLA-CH_4 spectrometer ($L = 3.60$ m) in the troposphere to lower stratosphere for mid-latitudes

Altitude (km)	P (mbar)	T (K)	ρ_{CH_4} (ppmv)	Absorption depth (%)	
				SDLA (1.65 μm)	DFG (3.24 μm)
0	1013	288.2	1.90	0.40	3.50
5	540.5	255.7	1.90	0.44	2.86
10	265	223.3	1.83	0.44	2.10
15	121.1	216.7	1.81	0.32	1.60
20	55.29	216.7	1.66	0.17	1.10
25	25.49	221.6	1.32	0.07	0.60
30	11.97	226.5	1.14	0.03	0.30

The precision can be improved by co-addition of successive measurements at the cost of a lower spatial resolution. Telecommunication laser diodes at 1.65 micron [9], lead-salt laser diode [10] or even quantum cascade lasers [11] emitting in the mid-infrared have been operated from balloons or aircrafts to monitor in situ CH_4 in the middle atmosphere. Due to the low concentration to be measured, these set-ups require a multi-path cell to expand the absorption path over a few tens of meters, making thereby the set-up heavy (the SDLA described in [9] has an overall weight of ~80 kg) and complex to operate. To develop a light-weight laser sensor (<5 kg) that can be operated even by a non-specialist, we have selected the 3.3 micron spectral region, which features the strong fundamental ν_3 band of methane. Over this spectral region interband cascade laser have been implemented recently [12]. For our part, we have selected an ultra-compact DFG laser emitting at 3.24 micron that was made available under a collaborative agreement from Novawave Technologies, Inc. Table 1 shows the comparison between absorption depths predicted for methane in the middle atmosphere at 1.65 and at 3.24 micron. At 3.24 micron, CH_4 can be measured over 3 m instead of 50 m at 1.65 micron, hence a multipass cell is no longer necessary. The absorption depth expected in the stratosphere is of 1% at 20 km which is largely feasible using the direct detection technique [13].

As a first step, we have checked the emission properties of the DFG laser and we have carefully revisited the intensities and the self-broadening coefficients of CH_4 in this spectral region for three specific manifolds particularly relevant for the CH_4 laser probing. The study was then extended to over 104 methane transitions also present in the tunability range of the DFG laser used. The first part of this paper reports the spectroscopic results. In the second part of the paper, we describe the balloon-borne DFG laser sensor called "PicoSDLA-CH4".

2 Experimental set-up

We used a Compact Difference Frequency Generation (CDFG) laser source provided by Novawave Technologies, Inc. (USA), as part of a collaborative agreement. The CDFG emits at 3086 cm^{-1} (3.24 μm) with a continuous coverage from 3076 to 3096 cm^{-1} (3.23 to 3.25 μm). The set-up developed by Novawave is compact (size of approximately 20 cm × 12 cm × 2.5 cm), of light weight (980 g) and it is therefore well-suited for balloon-borne deployments.

The DFG laser output power is 10 μW. A DFB laser diode at 1.5 μm (signal) is combined with the beam from a laser diode at 1 μm (the pump) using a silica fiber coupler. These elements are located in the CDFG laser module. Then, the beams are passed through a quasi-phase matching, periodically poled $LiNbO_3$ (PPLN) crystal which is located in the CDFG head. In the crystal, a non-linear effect produces radiation whose frequency is the difference between signal and pump frequencies. A germanium filter is used at the output of the laser to block the 1 and 1.5 μm radiation. The wavelength emission of the DFG laser can be changed by tuning the driving current and the temperature of the "signal" laser diode.

The line width is less than 10 MHz and the spectral emission does not feature any mode-hops over the tunability range which makes this source particularly convenient for spectroscopy. During preliminary tests, we have studied the response of the CDFG in terms of power and frequency according to the variations of the ambient temperature. For this purpose, in our laboratory, we thermally insulated the CDFG laser module and head in a box in which we made a temperature variation of 20°C. We observed a frequency shift of -0.005 cm^{-1}/Kelvin and a power variation of 2%/Kelvin. These tests demonstrated that the frequency and power excursions due to ambient temperature variations are rather limited. Anyway, we thermally controlled CDFG laser module and head to avoid spectral drifts during spectroscopic measurements in the laboratory and to have a better precision. In flight, a particular care will be taken to thermally control the CDFG laser module and head because of the severe environment encountered in the middle atmosphere.

The temperatures of the laser diodes (signal and pump) and of the Periodically Poled Lithium Niobate (PPLN) crystal are monitored as well as the power of the lasers using

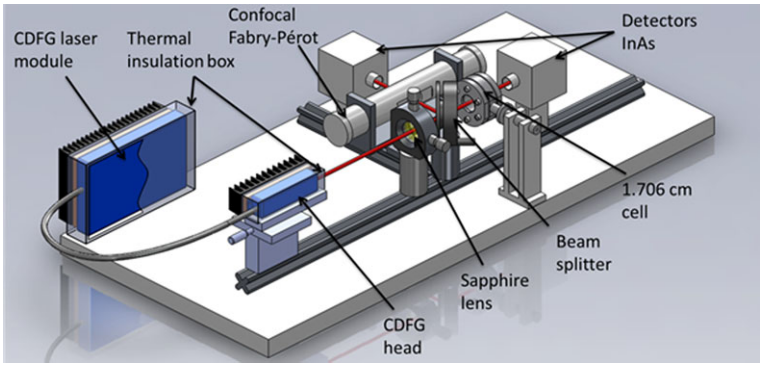

Fig. 1 Experimental set-up for CH_4 intensity and self-broadening coefficients measurements on R(5), R(6) and R(7) manifolds. To avoid some frequency shift and power variation during measurement, the CDFG head and the CDFG laser module are thermally insulated in a box with Peltier controllers

a PCMCIA DAQcard-6036E, with a resolution of 16 bits and a sampling rate of 200 ks/s. An NI USB-6251 card controlled by a LabVIEW 2009 program is used to control the emission wavelength over the selected molecular line shape. The duration of the ramp and consequently of a single spectrum is of 10 ms, and covers a scan of 1 cm^{-1}.

Figure 1 is a 3D-representation of the laboratory set-up used to record methane spectra with the CDFG laser source. The laser beam is focused by a sapphire convergent lens. A ZnSe beam splitter (R = 25%) is used to separate the laser beam into two parts. The first part passes through a 1.71 cm (accuracy: 1%) optical path length cell, and the reflected part is coupled to a confocal Fabry–Pérot interferometer (free spectral range of 9.45×10^{-3} cm^{-1}, uncertainty on wave number scale: 5.2×10^{-4} cm^{-1}) to obtain relative wave number calibration. The two beams are focused on two InAs photodiodes mounted with thermistors on two-stage thermoelectric coolers from Judson. The 1.71 cm-length single path cell was used to investigate the strong manifolds R(5), R(6) end R(7). Purposely, the 1.71 cm cell was filled with low pressure (between 0.1 and 2.5 mbar) of pure methane (99.9995%). The pressure was measured with an MKS Baratron manometer with 10 Torr full scale (accuracy: 0.25%) and the temperature of the gas is measured with a Platinium 4-wire PT 100 (tolerance: ±0.25°C at $T = 20$°C).

The spectroscopic work was then extended to numerous weak CH_4 lines that were present over the tunability range of the DFG laser. For this study, the optical path was expanded by replacing the 1.71 cm cell by a 20.4 cm long optical cell. The 20.4 cm cell was filled with 25 to 45 mbar pressure of pure methane (99.9995%). The pressure was measured with an MKS baratron manometer with 100 Torr full scale (accuracy: 0.25%). The temperature of the gas is measured with a Platinum 4-wire PT 100 (tolerance: ±0.25°C at $T = 20$°C).

An NI USB-6251 card, with a 16 bits resolution and a 1.25 Ms/s sampling rate per channel, is used to record simultaneously 2000 sample points from the signal and Fabry–Pérot channels.

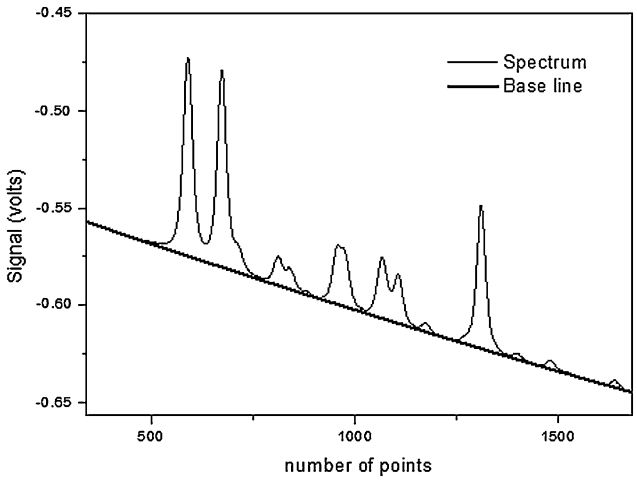

Fig. 2 Example of experimental spectrum recorded in this work at $P = 47.423$ mbar and $T = 297.7$ K (*thin line*) and the corresponding base line (*thick line*). The last was obtained by least squares fitting to a third-order polynomial

3 Data processing

To obtain the transmittance from the spectra we must, therefore, calculate the ratio between the recorded signal and its base line (I_0). To obtain the base line of the spectra we fit the points far enough of the line centers to a third order polynomial. In Fig. 2 we show an example of recorded spectrum and the corresponding base line given by the fit. In the recorded methane spectra, we can observe the contribution of the atmospheric CH_4 and H_2O outside the cell. In order to eliminate these contributions, we record a spectrum with the cell in vacuum for each one of the studied spectral regions, and we remove this contribution from the experimental spectrum.

We record one series of measurements (5–10 spectra) in about 5 minutes. For each series, a vacuum spectrum is recorded. We can consider that the humidity does not change significantly during this short period of time.

To calibrate the spectra in terms of frequency scale, a portion of the laser beam is sent to a confocal Fabry–Pérot (FP). The transmission of the FP is recorded simultaneously to

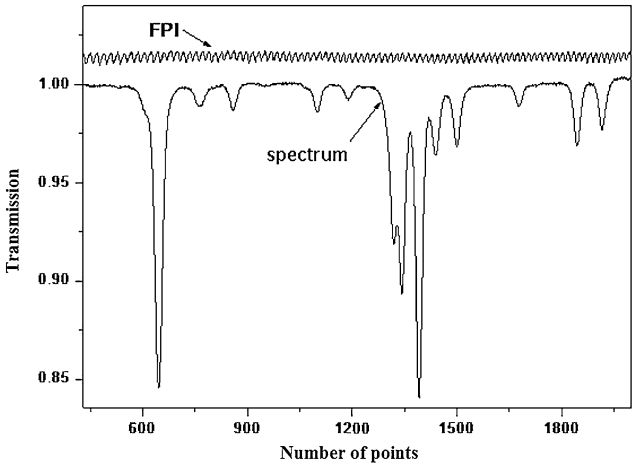

Fig. 3 Example of experimental spectrum of $^{12}CH_4$ recorded in this work at $P = 37.970$ mbar and $T = 297.5$ K, and the corresponding Fabry–Pérot transmission used for the calibration of the spectrum. They have been obtained using two portions of the same laser beam, and have been recorded simultaneously

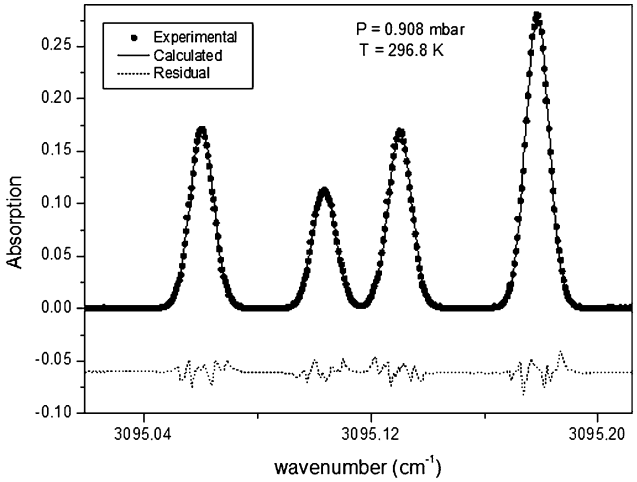

Fig. 4 Example of experimental spectrum of $^{12}CH_4$ recorded in this work at $P = 0.908$ mbar and $T = 296.8$ K (*solid circles*), the corresponding fit to Voigt profiles (*solid line*) and the residual between them (*dash line*). Residuals multiplied by 3 have been displaced for a better clarity

the absorption spectrum. The distance between two consecutive maximums of transmittance of a FP is given by its Free Spectral Range (FSR). In our case, the FSR of the used FPI is 9.45×10^{-3} cm^{-1} (the uncertainty on the wave number scale is 5.2×10^{-4} cm^{-1}). The uncertainty on the values of the wave number scale is determined from the number of points between two maximums.

To obtain the absolute wave number of the spectra, we take the position of the center of the strongest line from HITRAN database [14]. Then, we complete the wave number scale from the maximums of the FP transmission. Positions of the points between FP maximums are calculated using linear interpolation. In Fig. 3 we show an example of transmission spectrum and the corresponding FP transmission. The latter is displaced for a better clarity. Once the transmission spectra are calibrated in wave number, we obtain the transmission, τ, using the following simple relationship:

$$\tau = \frac{I}{I_0} = \exp\left(S(T)\rho_{\text{act}} \frac{L}{\gamma_D} \sqrt{\frac{\ln(2)}{\pi}} \Re\big[w(x,y)\big] \frac{P}{k_B T} \right) \quad (1)$$

$$w(x,y) = \frac{i}{\pi} \int_{-\infty}^{\infty} \frac{\exp(-t^2)}{x - t + iy}\, dt \quad (2)$$

Here $w(x, y)$ is the complex probability or error function, L is the gas cell length (cm), γ_D the Doppler broadening parameter (cm^{-1}), and $S(T)$ the line intensity (from HITRAN database).

The variables x and y are defined according to

$$x = \frac{\sigma - \sigma_0}{\gamma_D} \sqrt{\ln(2)} \quad \text{and} \quad y = \frac{\gamma_L}{\gamma_D} \sqrt{\ln(2)} \quad (3)$$

with σ_0 the transition frequency (cm^{-1}), σ the wave number (cm^{-1}), γ_L the Lorentz broadening parameter (cm^{-1}), ρ_{act} the mixing ratio of the active molecule.

Then, the intensities and collisional broadening of the lines are obtained from the fit of the lines to a Voigt profile. In this fit, the Doppler width, γ_D, is considered as constant for the entire record, (remember that the length of each spectrum is about 1 cm^{-1}). Note that due to the low pressure range used in our measurement, line-mixing effects are not expected to be observed in these spectra.

In Fig. 4 we show an example of recorded spectrum and its corresponding Voigt fit. The residual have been displaced for the sake of clarity. Finally, the intensities, S, which were recorded at different temperatures (between 295 and 298 K), are standardized to $T = 296$ K using the following equation:

$$S(T_0) = S(T) \frac{Q(T)}{Q(T_0)} \exp\left[\frac{-hcE_0}{k_B} \left(\frac{1}{T_0} - \frac{1}{T} \right) \right] \quad (4)$$

Here T_0 is the temperature of reference (296 K) and k_B is the Boltzmann constant, E_0 is the energy of the lower level of the transition in cm^{-1} and Q is total internal partition sum. Q is calculated using the code described in [15].

4 Results and discussion

In a first step, to test the quality of our spectra and of the data processing, we have measured the intensities of the three manifolds R(5), R(6) and R(7) belonging to the ν_3 band. We have compared these data with those of HITRAN, which were obtained by Fourier Transform Spectroscopy (FTS) [16], and those of Pine [17], who used a difference-frequency laser spectrometer. For each of the two studies,

Table 2 Comparison between the intensity values from the work of Pine [17] (column c), HITRAN (column d) and this work (column e), for the R(5), R(6) and R(7) manifolds of the ν_3 band of $^{12}CH_4$. In column (**a**), prime and double prime refer, respectively, to upper and lower states. J is the quantum number associated with the total angular momentum, C is the quantum number corresponding to A_1, A_2, F_1, F_2 and E described in [16], and α is a counting integer, increasing with energy, for levels with the same J and C. Column (**b**) corresponds to the HITRAN line positions. Column (**f**) corresponds to the relative difference between the values of the intensities obtained in this work and those of Pine. Column (**g**) corresponds to the relative difference between the values of the intensities obtained in this work and those of HITRAN

Line Branch$(J'')C'C''\alpha'\alpha''$	Position (cm^{-1})	$S(T_0)$ (cm^{-1}/molecule cm^{-2}) [Pine [17]]	$S(T_0)$ (cm^{-1}/molecule cm^{-2}) [HITRAN]	$S(T_0)$ (cm^{-1}/molecule cm^{-2}) [This work]	Rel. diff. (%)	Rel. diff. (%)
(a)	(b)	(c)	(d)	(e)	(f)	(g)
R(5)f2f1α23α2	3076.549659	(1.200 ± 0.003) E–19	(1.166 ± 0.032) E–19	(1.291 ± 0.004) E–19	−7.6	−10.7
R(5) eeα1α1	3076.569031	(8.117 ± 0.021) E–20	(7.795 ± 0.019) E–20	(7.000 ± 0.048) E–20	13.8	10.2
R(5) f1f2α21α1	3076.677108	(1.195 ± 0.003) E–19	(1.156 ± 0.029) E–19	(1.117 ± 0.004) E–19	6.5	3.4
R(5) f2f1α24α1	3076.725178	(1.194 ± 0.003) E–19	(1.166 ± 0.029) E–19	(1.146 ± 0.004) E–19	4.0	1.7
R(6) a2a1α10α11	3085.832038	(1.744 ± 0.004) E–19	(1.680 ± 0.042) E–19	(1.708 ± 0.006) E–19	2.1	−1.7
R(6) f2f1α25α11	3085.861015	(1.041 ± 0.002) E–19	(1.010 ± 0.025) E–19	(1.029 ± 0.004) E–19	1.2	−1.9
R(6) f1f2α26α2	3085.893769	(1.043 ± 0.002) E–19	(1.010 ± 0.025) E–19	(1.065 ± 0.003) E–19	−2.1	−5.4
R(6) a1a2α8α21	3086.030985	(1.697 ± 0.004) E–19	(1.650 ± 0.041) E–19	(1.731 ± 0.005) E–19	−2.0	−4.9
R(6) f1f2α27α1	3086.071879	(1.037 ± 0.002) E–19	(9.920 ± 0.24) E–20	(1.007 ± 0.003) E–19	2.9	−1.5
R(6) eeα17α1	3086.085994	(6.917 ± 0.015) E–20	(6.620 ± 0.16) E–20	(6.520 ± 0.002) E–20	5.7	1.5
R(7) f2f1α29α2	3095.060894	(8.362 ± 0.035) E–20	(8.102 ± 0.20) E–20	(8.061 ± 0.020) E–20	3.6	0.5
R(7) eeα20α1	3095.104039	(5.537 ± 0.023) E–20	(5.375 ± 0.13) E–20	(5.405 ± 0.053) E–20	2.4	−0.6
R(7) f1f2α28α2	3095.130721	(8.333 ± 0.035) E–20	(8.042 ± 0.20) E–20	(7.927 ± 0.036) E–20	4.9	1.4
R(7) a1a2α11α1	3095.179340	(1.370 ± 0.006) E–19	(1.344 ± 0.034) E–19	(1.331 ± 0.005) E–19	2.8	1.0
R(7) f1f2α29α1	3095.351550	(8.163 ± 0.034) E–20	(7.914 ± 0.019) E–20	(8.201 ± 0.051) E–20	−0.5	−3.6
R(7) f2f1α30α1	3095.371363	(8.146 ± 0.034) E–20	(7.934 ± 0.019) E–20	(7.889 ± 0.035) E–20	3.2	0.6

the range of pressures has been chosen to avoid line-mixing effects on spectra. As shown in Table 2, our results are in good agreement with both Pines' and HITRAN measurements, with a relative difference of less than 5% in most of the cases. Moreover, 10 of 16 of our intensity values are included in the error bar of the HITRAN database, in which standard error reported for the pentad ν_3 band is on average 2.5%. Only three lines of R(5) manifold present a bigger relative difference from those of HITRAN or Pine, but remember that we can observe an overlapping with atmospheric H_2O line in this part of the spectra, which complicates the determination of the base line, and therefore the determination of the intensities. We have subtracted the atmospheric contribution from our spectra to avoid problems in the determination of the base line. However, no mention about that is made in any of the others two cited works, so we suppose that the reason for the observed disagreement with our data is that this contribution has not been observed or because it has not been taken into account in the corresponding fits in references [16, 17]. Another possible source of error, in both the work of Pine and our work, is the fact that we have not taken into account in the fit some weak (methane) lines in the same spectral region under study, what can give rise to an incorrect base line determination.

In a second step, the self-collisional broadening and intensity of 104 lines belonging to seven different bands in the spectral interval between 3077.4 and 3094.5 cm^{-1} have been obtained. The intensities of these lines in HITRAN come from [15] for the ν_1, ν_3, $\nu_2+\nu_4$ and $2\nu_2$ bands, and [18] for the $\nu_1+\nu_4-\nu_4$, $\nu_3+\nu_4-\nu_4$ and $\nu_2+\nu_3-\nu_2$ bands. Both of them used Fourier Transform spectrometer. In this work we present the intensities measured with difference-frequency laser spectrometer, which has a negligible apparatus function compared to FTIR instrument typically used for this kind of measurement and hence the determination of the apparatus function is not necessary. Due to a lack of experimental self-broadening data, most of the values in HITRAN were obtained with a simple empirical expression [19]. In this work we present new experimental measurements of the self-broadening of the considered lines.

In total, we have studied 17 different spectral regions, 1 cm^{-1} long (the length of one spectrum), including the three manifolds R(5), R(6) and R(7). For each of them, we have recorded between 5–10 spectra, which were averaged on 100 spectrums, at different pressures (0.1–2.5 mbar for the manifolds and 25–45 mbar for the rest of the lines) and temperatures varying between 295 and 298 K. All the intensity values have, however, been standardized at 296 K. In Tables 2 and 3 we show the corresponding results. The

Table 3 Line intensities and self-broadening of $^{12}CH_4$ obtained in this work. The uncertainties are standard errors. In the first column at left, prime and double prime refer, respectively, to upper and lower states. J is the quantum number associated with the total angular momentum, C is the quantum number corresponding to A_1, A_2, F_1, F_2 and E described in [16], and α is a counting integer, increasing with energy, for levels with the same J and C. Line positions are those of HITRAN

Line Branch$(J'')C'C''\alpha'\alpha''$	Position (cm^{-1})	S (cm^{-1}/molecule cm^{-2})	Self-broadening (cm^{-1}/atm)
ν_1			
R(16) a2a1α49α2	3077.58782	(1.353 ± 0.050) E–23	0.078 ± 0.006
ν_3			
R(5) eeα16α1	3079.23446	(4.153 ± 0.439) E–23	0.053 ± 0.008
R(5) f1f2α22α1	3079.27629	(9.728 ± 0.161) E–23	0.060 ± 0.007
R(5) f1f2α23α1	3080.03687	(1.267 ± 0.005) E–21	0.096 ± 0.003
R(5) f2f1α25α1	3080.16292	(4.875 ± 0.177) E–22	0.057 ± 0.020
R(5) f2f1α26α1	3083.72227	(5.156 ± 0.045) E–22	0.101 ± 0.002
R(5) f1f2α1α25	3084.42012	(2.079 ± 0.068) E–23	0.070 ± 0.004
R(5) f2f1α27α2	3084.45828	(9.655 ± 0.083) E–23	0.107 ± 0.002
R(6) f2f1α26α1	3088.82349	(2.793 ± 0.032) E–23	0.053 ± 0.004
R(6) f1f2α28α2	3088.87204	(4.215 ± 0.037) E–23	0.084 ± 0.001
R(6) f1f2α28α1	3088.89374	(3.081 ± 0.070) E–23	0.075 ± 0.002
R(6) a1a2α9α1	3089.73234	(3.307 ± 0.002) E–21	0.111 ± 0.007
R(6) f1f2α29α2	3089.86809	(2.293 ± 0.029) E–22	0.109 ± 0.014
R(6) f1f2α29α1	3089.88979	(1.161 ± 0.012) E–21	0.139 ± 0.027
R(6) eeα18α1	3089.98981	(6.707 ± 0.066) E–22	0.136 ± 0.018
R(6) f1f2α30α1	3094.14584	(2.929 ± 0.014) E–22	0.090 ± 0.003
R(6) eeα19α1	3094.21602	(2.552 ± 0.032) E–22	0.083 ± 0.004
$\nu_1 + \nu_4 - \nu_4$			
R(8) eeα39α1	3092.21954	(1.148 ± 0.011) E–23	0.059 ± 0.002
R(8) f1f2α60α1	3092.42098	(3.187 ± 0.046) E–23	0.088 ± 0.003
$\nu_3 + \nu_4 - \nu_4$			
R(6) f2f1α64α5	3078.84180	(7.312 ± 0.451) E–23	0.036 ± 0.014
R(6) f2f1α62α4	3079.09110	(1.307 ± 0.014) E–22	0.085 ± 0.004
R(6) eeα43α3	3079.18500	(9.239 ± 0.208) E–23	0.057 ± 0.005
R(6) f1f2α64α4	3079.22350	(1.579 ± 0.058) E–22	0.082 ± 0.006
R(6) f2f1α65α5	3081.86879	(6.482 ± 3.928) E–23	0.075 ± 0.004
R(7) f2f1α56α2	3082.31380	(1.552 ± 0.018) E–22	0.074 ± 0.002
R(7) eeα37α1	3082.34000	(1.034 ± 0.013) E–22	0.068 ± 0.002
R(6) a2a1α24α2	3083.47200	(7.603 ± 0.089) E–23	0.075 ± 0.002
R(7) f2f1α61α3	3085.08600	(1.307 ± 0.051) E–22	0.064 ± 0.002
R(7) eeα50α4	3087.32813	(3.793 ± 0.060) E–23	0.067 ± 0.002
R(7) f2f1α75α6	3087.60500	(9.760 ± 0.108) E–23	0.089 ± 0.001
R(7) f1f2α71α4	3087.64545	(1.185 ± 0.014) E–22	0.081 ± 0.002
R(7) f2f1α73α5	3087.69550	(1.301 ± 0.005) E–22	0.116 ± 0.003
R(6) f2f1α67α4	3088.49293	(6.927 ± 0.444) E–24	0.121 ± 0.019
R(8) f2f1α60α2	3091.73770	(7.062 ± 0.302) E–24	0.058 ± 0.005
R(7) f1f2α74α5	3091.96803	(6.532 ± 0.169) E–24	0.052 ± 0.004
R(7) f2f1α76α6	3092.45291	(2.916 ± 0.062) E–23	0.085 ± 0.004
R(8) a2a1α22α1	3093.44470	(1.379 ± 0.009) E–22	0.081 ± 0.002
R(7) a1a2α27α2	3093.77251	(8.993 ± 0.145) E–23	0.081 ± 0.007
R(8) eeα44α2	3094.08340	(7.027 ± 0.159) E–23	0.057 ± 0.003
R(8) f1f2α68α3	3094.09700	(1.203 ± 0.023) E–22	0.086 ± 0.008
R(7) f1f2α76α5	3094.17668	(2.208 ± 0.094) E–23	0.114 ± 0.021
R(8) f2f1α68α4	3094.25175	(1.971 ± 0.139) E–23	0.042 ± 0.009
R(7) f2f1α77α6	3094.33882	(5.318 ± 0.545) E–24	0.005 ± 0.001
R(8) f1f2α70α4	3094.42929	(9.973 ± 0.161) E–23	0.064 ± 0.009
R(8) f2f1α67α3	3094.51237	(1.062 ± 0.042) E–22	0.075 ± 0.013

Table 3 (*Continued*)

Line Branch$(J'')C'C''\alpha'\alpha''$	Position (cm^{-1})	S (cm^{-1}/molecule cm^{-2})	Self-broadening (cm^{-1}/atm)
$\nu_2+\nu_4$			
R(13) f2f1α48α1	3078.74288	(1.955 ± 0.108) E–22	0.068 ± 0.019
R(14) a2a1α18α1	3082.45932	(5.113 ± 0.081) E–23	0.056 ± 0.002
R(14) f2f1α50α1	3087.41754	(5.340 ± 0.110) E–23	0.049 ± 0.002
R(15) a2a1α17α1	3088.68712	(1.093 ± 0.058) E–23	0.041 ± 0.008
$\nu_2+\nu_3-\nu_2$			
R(6) f2f1α91α8	3078.97055	(1.508 ± 0.086) E–23	0.020 ± 0.004
R(7) f1f2α98α9	3083.03211	(1.841 ± 0.038) E–23	0.090 ± 0.004
R(7) f2f1α102α9	3083.43125	(1.323 ± 0.019) E–23	0.062 ± 0.002
R(7) f2f1α107α9	3089.10193	(5.300 ± 0.201) E–24	0.064 ± 0.005
R(8) f1f2α112α11	3091.81422	(4.277 ± 0.147) E–24	0.067 ± 0.004
R(8) f2f1α111α10	3092.09696	(1.044 ± 0.015) E–23	0.050 ± 0.004
R(8) a1a2α36α4	3092.65306	(2.594 ± 0.032) E–23	0.050 ± 0.004
R(8) f2f1α113α10	3093.50015	(8.644 ± 0.312) E–24	0.055 ± 0.005
R(8) a2a1α40α4	3093.93073	(8.458 ± 0.561) E–24	0.048 ± 0.011
$2\nu_2$			
Q(9) f2f1α40α3	3077.24614	(8.581 ± 0.328) E–24	0.045 ± 0.003
Q(7) f1f2α36α2	3077.39141	(1.342 ± 0.006) E–22	0.088 ± 0.003
Q(7) f1f2α36α1	3077.42951	(2.956 ± 0.018) E–23	0.072 ± 0.002
Q(7) eeα23α1	3077.49121	(6.306 ± 0.082) E–23	0.095 ± 0.005
Q(10) f1f2α43α3	3077.69264	(5.838 ± 0.274) E–24	0.041 ± 0.005
Q(10) eeα30α2	3077.77776	(8.036 ± 0.151) E–24	0.035 ± 0.004
Q(10) a1a2α16α1	3077.81043	(6.783 ± 0.111) E–23	0.070 ± 0.002
Q(10) f1f2α43α1	3077.92544	(3.098 ± 0.114) E–23	0.069 ± 0.006
Q(10) eeα30α1	3077.99846	(1.974 ± 0.073) E–23	0.076 ± 0.006
Q(10) f2f1α46α2	3078.66408	(1.795 ± 0.096) E–23	0.044 ± 0.012
Q(8) f2f1α39α1	3078.80039	(3.234 ± 0.246) E–22	0.042 ± 0.014
Q(11) f2f1α48α1	3079.96464	(1.910 ± 0.040) E–23	0.011 ± 0.002
Q(11) f1f2α49α1	3080.00107	(3.826 ± 0.065) E–23	0.027 ± 0.008
Q(8) f2f1α40α2	3080.38381	(8.991 ± 0.110) E–23	0.102 ± 0.007
Q(8) f2f1α40α1	3080.45491	(2.190 ± 0.050) E–23	0.093 ± 0.023
Q(8) f1f2α37α1	3080.59528	(1.870 ± 0.016) E–22	0.094 ± 0.005
Q(9) f1f2α44α1	3081.78901	(2.451 ± 0.443) E–22	0.060 ± 0.012
Q(9) a2a1α16α1	3083.37909	(1.052 ± 0.007) E–22	0.076 ± 0.002
Q(12) f2f1α54α2	3083.51082	(2.124 ± 0.029) E–23	0.105 ± 0.007
Q(9) eeα28α1	3084.10461	(9.420 ± 0.076) E–23	0.074 ± 0.001
Q(9) f1f2α45α2	3084.75788	(2.295 ± 0.046) E–23	0.055 ± 0.002
Q(9) f2f1α43α3	3084.83642	(2.675 ± 0.072) E–23	0.056 ± 0.002
Q(9) f2f1α43α2	3084.88622	(3.505 ± 0.046) E–23	0.068 ± 0.001
Q(9) a1a2α14α1	3084.91039	(3.689 ± 0.132) E–23	0.098 ± 0.008
Q(10) a1a2α17α1	3085.06790	(6.908 ± 0.907) E–24	0.028 ± 0.009
Q(10) eeα32α1	3085.16882	(1.318 ± 0.025) E–22	0.072 ± 0.002
Q(10) f2f1α48α2	3087.06542	(7.880 ± 0.535) E–24	0.107 ± 0.013
Q(10) f2f1α48α1	3087.14090	(5.642 ± 0.055) E–23	0.082 ± 0.002
R(1) f2f1α13α1	3087.27135	(2.058 ± 0.059) E–23	0.053 ± 0.003
Q(11) f1f2α52α1	3088.62584	(1.414 ± 0.006) E–22	0.063 ± 0.001
Q(11) f2f1α50α1	3088.66712	(1.359 ± 0.016) E–22	0.061 ± 0.001

Table 3 (*Continued*)

Line Branch(J'')$C'C''\alpha'\alpha''$	Position (cm^{-1})	S (cm^{-1}/molecule cm^{-2})	Self-broadening (cm^{-1}/atm)
Q(10) f2f1α49α2	3088.73717	(1.506 ± 0.021) E–23	0.043 ± 0.003
Q(10) f1f2α47α3	3088.75344	(1.167 ± 0.058) E–23	0.056 ± 0.007
Q(10) f2f1α49α1	3088.81265	(2.932 ± 0.067) E–23	0.050 ± 0.005
Q(10) a2a1α15α1	3089.00506	(9.688 ± 0.080) E–23	0.073 ± 0.001
Q(15) f2f1α64α1	3089.05790	(2.073 ± 0.105) E–24	0.015 ± 0.004
Q(11) eeα34α1	3091.10960	(2.632 ± 0.039) E–23	0.058 ± 0.002
Q(11) f1f2α53α3	3091.12366	(6.477 ± 0.371) E–24	0.117 ± 0.009
Q(11) f1f2α53α2	3091.26439	(4.354 ± 0.033) E–23	0.083 ± 0.001
Q(12) eeα37α1	3092.34862	(4.834 ± 0.165) E–24	0.032 ± 0.006
Q(12) f2f1α56α1	3092.36224	(7.653 ± 0.192) E–23	0.052 ± 0.004
Q(12) a2a1α18α1	3092.39015	(1.405 ± 0.009) E–22	0.061 ± 0.001
Q(11) f1f2α54α3	3092.55533	(8.544 ± 0.388) E–24	0.056 ± 0.005
Q(11) f1f2α54α2	3092.69603	(1.817 ± 0.070) E–23	0.038 ± 0.009
Q(11) eeα35α2	3093.04635	(3.464 ± 0.153) E–24	0.010 ± 0.001
Q(11) f2f1α52α2	3093.27684	(3.937 ± 0.027) E–23	0.093 ± 0.004

wave numbers in the table correspond to the HITRAN line positions, and both intensity and collisional broadening are expressed in the same units as HITRAN. In order to compare with values reported by Pine, for each line in the tables, the error is calculated as the standard error, *se*, given by the ratio between the standard deviation, σ, and the square root of the number of spectra, N:

$$se = \frac{\sigma}{\sqrt{N}} \tag{5}$$

Nevertheless, the *se* corresponds to random experimental errors (uncertainties on pressure, temperature, etc.) and underestimates the total error. We must also take into account the error of the fit. We have estimated this error by calculating the difference between the maximum and minimum of the main structure of the residual, and compare this value with the maximum of the considered line. This way we obtain a value of about 2%. Being this error much bigger than the *se*, we can consider it as a good estimation of the intensity total uncertainty.

Thus, we have obtained accurate intensity values of these 104 lines using DFG spectroscopy for the first time. We have also determined the corresponding self-broadening coefficients, which have never been measured before. Figure 5 shows results of fitting procedure on three spectra at different pressures.

Moreover, intensities and self-broadening coefficients made on the R(6) manifold will be used for the processing of the in situ methane absorption spectra acquired by the balloon-borne spectrometer described in the next section.

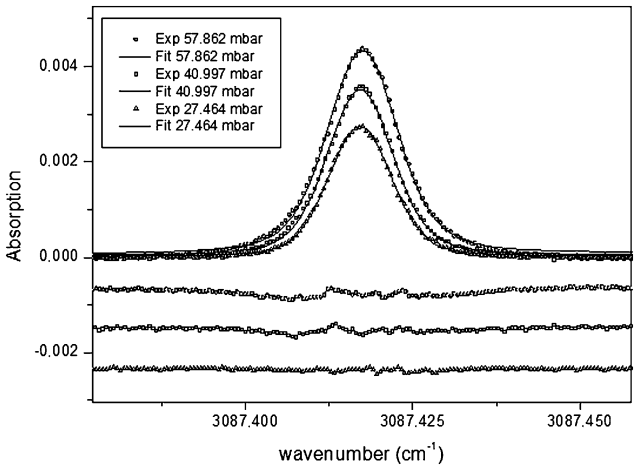

Fig. 5 Absorption spectra on the $\nu_2 + \nu_4$ band R(14) line of pure CH_4 at different pressures (*open circles, open squares* and *open triangles*), the corresponding fit (*solid line*) and residuals are displaced for better visibility

5 The balloon-borne "PicoSDLA-CH_4" spectrometer

As discussed above, strong absorption lines in the ν_3 band region allow one to measure CH_4 in the middle atmosphere with a short optical path length. Figure 6 features the absorption spectra of H_2O and CH_4 calculated for an absorption path length of 3.6 m at ground level for the selected spectral region at 3086 cm^{-1} (3.24 μm). To avoid overlapping with water vapor lines in the lower troposphere, we have selected the R(6) transition of the ν_3 band to monitor atmospheric methane.

Figure 7 is a 3D-representation of the PicoSDLA-CH_4 balloon-borne sensor. The sensor design is based on the "PicoSDLA-H_2O" laser hygrometer described in [20]. The laser beam is propagated in the open atmosphere over an absorption path length of ∼3.6 m and is partially absorbed in situ by the ambient CH_4 molecules. The laser beam of the DFG laser is collimated by a plano-convex sapphire lens. The beam passes through the open atmosphere and is reflected by a gold-coated retro-reflector with a diameter of 63.5 mm. Then, the laser beam is focused by another sapphire lens to an InAs photodiode (Judson Inc.).

With the PicoSDLA, the wavelength laser emission is tuned over the R(6) manifold by ramping of the laser driving current in 10 ms. Over each elementary 10 ms-spectrum, 512 sample points are taken with a 16 digits sampler. A great care has been taken in the thermal protection of the CDFG laser to avoid spectral drift as the sensor will be operated in a severe environment in terms of temperature (at 10 km the temperature may be as low as −70°C) and pressure (at 30 km, the pressure is ∼10 hPa). As mentioned above, we have carried out numerous tests in the laboratory to check out the behavior of the CDFG laser with ambient temperature. The temperature of the laser environment is controlled accordingly during the flight using heaters. Similarly, the lenses and the retro-reflector are heated to avoid the formation of ice.

Figure 8 is a picture of the sensor prototype as deployed during the balloon campaign in Kiruna (northern Sweden,

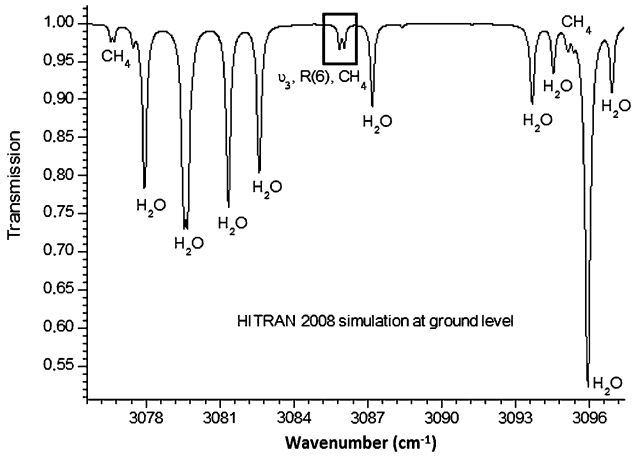

Fig. 6 Simulated spectrum in atmospheric conditions at ground level for water vapor and methane lines on the spectral range from 3077 to 3095 cm^{-1}. The *black square* show the R(6) manifold selected for in situ measurements of methane with the PicoSDLA-CH_4 spectrometer

Fig. 8 Picture of the PicoSDLA-CH_4 sensor during the balloon campaign in Kiruna, Sweden, in March–April 2011

Fig. 7 Schematic of the PicoSDLA-CH_4 spectrometer

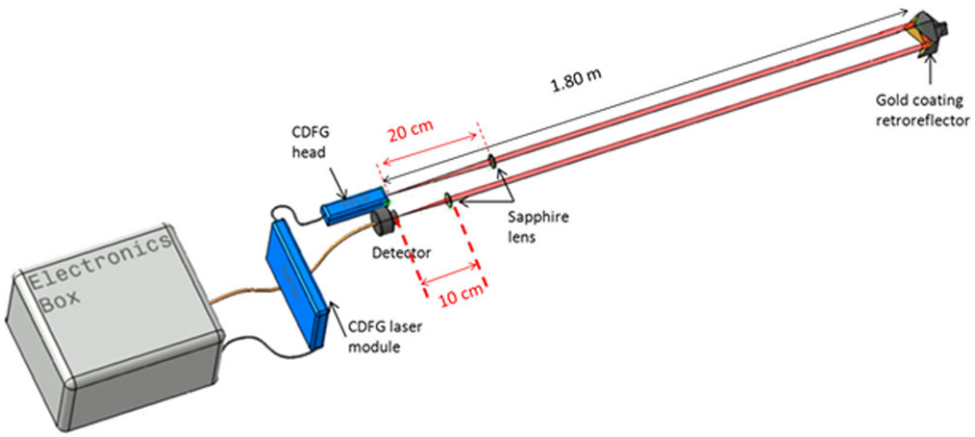

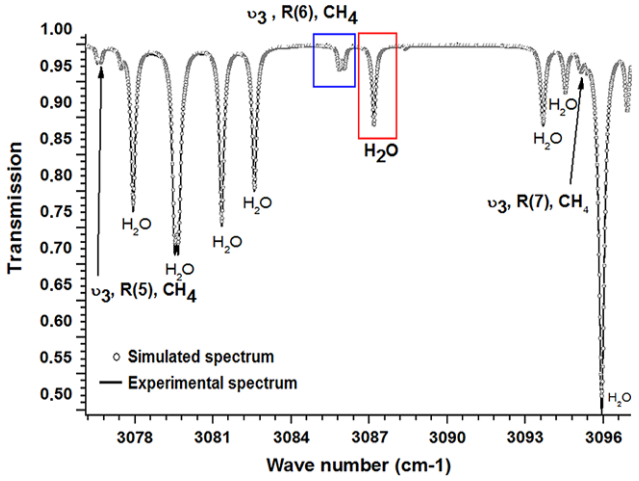

Fig. 9 Calculated spectrum of water vapor and methane (*open gray circles*) and experimental spectrum (*black line*) from 3076 to 3096 cm^{-1}. Pressure is 1001.1 mbar, temperature is 22.8°C, the optical path length is 355 cm

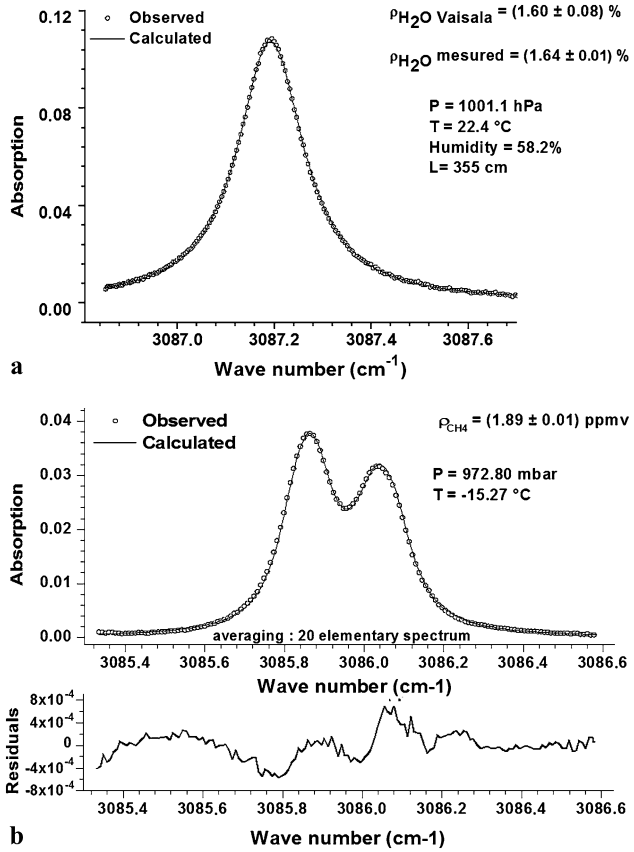

Fig. 10 Experimental spectrum of water vapor (**a**) (*open circles*) obtained during measurements with the PicoSDLA-CH_4 spectrometer. Data processing (*black line*) was achieved applying non-linear least-square fitting procedure with Voigt profile. The humidity was recorded with Vaisala weather transmitter for comparison. (**b**) CH_4 absorption spectrum (*open circles*) featuring the R(6), ν_3 transition, obtained with the PicoSDLA-CH_4 sensor in ambient air. The optical path length was 355 cm in the open atmosphere

65°N) in March–April 2011; the laser sensor was installed as a piggy-back in a larger gondola (the TWIN experiment, PI Dr. A. Engels, University of Frankfurt) to be test-flown. The structure of the cell is made of carbon fiber tubes. The atmospheric pressure and temperature are recorded using a small pressure gauge (Honeywell, 0.01 hPa precision error) and three meteorological thermistors (VIZ, 0.1°C precision). The overall weight of this prototype (including the lithium batteries) is of ∼8 kg.

Figure 9 shows the experimental spectrum of ambient air at ground level featuring CH_4 and H_2O transitions from 3076 to 3096 cm^{-1}(black line). It consists of a juxtaposition of 16 experimental spectra of 1 cm^{-1} spectral range each. Each spectrum was obtained in 10 ms by applying the appropriate temperature and driving current to the laser.

Figure 10(a) is a zoom on the H_2O line at 3087.20 cm^{-1} in Fig. 9. We processed this H_2O spectrum by applying a Levenberg–Marquardt non-linear least-squares fitting with a Voigt profile. To assert the reliability of this H_2O measurement, we have monitored simultaneously the humidity with a Vaisala weather sonde (WTX 510 Weather transmitter, humidity accuracy: ±3% RH). The mixing ratio measured by the Vaisala weather sonde during the recording of this spectrum was $1.60 \pm 0.08\%$. The mixing ratio obtained from the fitting procedure is $1.64 \pm 0.01\%$. Both H_2O measurements are in very good agreement.

A long set of methane measurements was done at ground level to assess the dispersion of the methane concentration. The CH_4 spectrum in Fig. 10(b) was processed by applying a non-linear least-square fitting procedure including line-mixing effects [22, 23] and by means of the molecular parameters reported in this work. The yielded CH_4 concentration is of 1.89 ± 0.01 ppmv at ground level.

The PicoSDLA was test-flown on the first of April, 2011 from Kiruna. The stratospheric balloon reached a float altitude of nearly 20 km before starting a slow descent in the lower stratosphere. During the descent, the measurements in the troposphere were obtained under large parachutes. The overall duration of the flight was of 3 hours. Figure 11 reports elementary spectra recorded at various altitude within 10 ms. The dispersion in the methane mixing-ratio measurements reported in Figs. 11(b) and 11(c), of the order of ±0.03 ppmv, was done by fitting successive 10 ms-spectra while the sensor was descending slowly in the atmosphere (at a few m/s), and by assuming that the atmospheric pressure and temperature were nearly constant over a one second period of time. The measured absorption depths are in good agreement with the predictions in Table 1.

Hence, at 20 km, the absorption depth is of ∼1% and the noise observed in the spectrum is of $\sim 10^{-3}$ expressed in absorption unit for a measurement time of 10 ms as featured in Fig. 11(a). Successive elementary 10-ms spectra can be

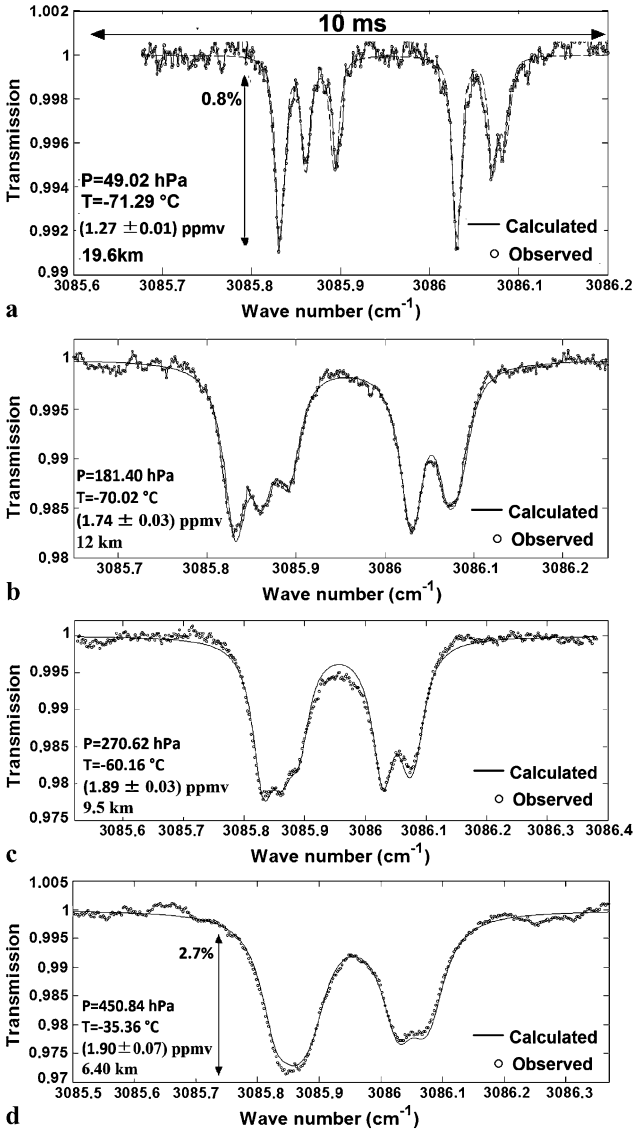

Fig. 11 In situ methane spectra at 19.6 km (**a**), 12 km (**b**), 9.5 km (**c**) and 6.4 km (**d**) achieved during the balloon flight of the PicoSDLA-CH_4 on the 1st of April 2011, in Kiruna, Sweden. The measurement time is of 10 ms. See text for more details

co-added to improve further the signal to noise ratio. The expected temporal resolution for these atmospheric applications under balloon platforms is of one second, corresponding to the co-addition of roughly hundred 10-ms elementary spectra. Taking into account the achievable precision errors in atmospheric temperature (∼0.1°C), pressure (0.01 hPa) and in baseline determination (1%) and considering the precision errors in the methane line strengths reported in this paper as well as the noise featured in the atmospheric spectra ($\sim 10^{-4}$ expressed in absorption unit), we obtain a precision error of roughly 5%, up to 20 km for a measurement time of 1 s. It is possible to further enhance the precision by co-adding successive CH_4 concentration data but at the cost of a lower spatial resolution in the vertical profile.

The DFG laser has operated flawlessly despite the severe environment encountered during the flight. The full set of spectra is still under processing using the molecular parameters reported in this work and will be compared, in a next step, to the CH_4 data yielded by the cryosampler operated onboard the TWIN gondola.

6 Conclusion

To test the performance of the DFG source as a spectroscopic tool, we have made some measurements to determine the R(5), R(6) and R(7) manifolds intensities and self-broadening parameters, and compared with HITRAN 2008 values. These spectroscopic parameters will be further used for data processing of atmospheric spectra. The results obtained are in good agreement with HITRAN values. Then, we realized a spectroscopic study covering seven bands of methane in the spectral region from 3077 to 3095 cm^{-1} to determine the intensities and self-broadening of 104 lines. Most of the intensities have been measured by difference-frequency laser spectrometer for the first time, and we present new experimental self-broadening values for most of the lines. It is noted that the temperature dependence of the air pressure-broadening coefficients has also been studied in the laboratory with the DFG, but these data will be the subject of a separate forthcoming spectroscopic paper.

The DFG laser source was used to develop a balloon-borne methane sensor based on a single path in the open atmosphere over ∼3 m. Preliminary measurements of methane achieved during the test-flight of the instrument show a good agreement with the science objective in terms of precision error and measurement time. The flight demonstrated the suitability of the DFG laser for atmospheric soundings, despite a severe atmospheric environment.

In a next step, following the test-flight, we will go further in the reduction of the weight of the current prototype. Indeed, the "PicoSDLA-CH_4" spectrometer will be one of the major tools of the "TRO-Pico" balloon campaign scheduled at the beginning of 2012 in Brazil and focused on the study of the impact of convection on the tropical lower stratosphere.

Acknowledgements We thank Jean Michel Hartmann and Ha Tran for scientific discussion about line-mixing and the CNES balloon department for its involvement in the test-flight. We thanks Jean-Christophe Samaké, Fabien Frérot, Louis Rey Grange, Christophe Berthod (DT-INSU (CNRS)) and Patrick Poinsignon (LATMOS) for the balloon-borne sensor development. The work described in this paper was supported by the CNRS, the CNES and the Région Champagne Ardenne.

References

1. P. Forster, V. Ramaswamy, P. Artaxo, T. Berntsen, R. Betts, D.W. Fahey, J. Haywood, J. Lean, D.C. Lowe, G. Myhre, J. Nganga,

R. Prinn, G. Raga, M. Schulz, R. Van Dorland, in *Climate Change 2007: The Physical Science Basis. Contribution of Working Group I to the Fourth Assessment Report of the Intergovernmental Panel on Climate Change*, ed. by S. Solomon, D. Qin, M. Manning, Z. Chen, M. Marquis, K.B. Averyt, M. Tignor, H.L. Miller (Cambridge University Press, Cambridge, 2007)
2. R. Delmas, G. Megie, V.H. Peuch, *Physique et chimie de l'atmosphère*. Ed. Belin (2005)
3. M. Rigby, R.G. Prinn, P.J. Fraser, P.G. Simmonds, R.L. Langenfelds, J. Huang, D.M. Cunnold, L.P. Steele, P.B. Krummel, R.F. Weiss, S. O'Doherty, P.K. Salameh, H.J. Wang, C.M. Harth, J. Mühle, L.W. Porter, Geophys. Res. Lett. **35**, L22805 (2008)
4. K.M. Walter, S.A. Zimov, J.P. Chanton, D. Verbyla, F.S. Chapin III, Nature **443**, 71 (2006)
5. G. Durry, A. Hauchecorne, Atmos. Chem. Phys. **5**, 1467 (2005)
6. D.T. Shindell, D. Rind, P. Lonergan, Nature **392**, 589 (1998)
7. R.L. Herman, K. Drdla, J.R. Spackman, D.F. Hurst, P.J. Popp, C.R. Webster, P.A. Romashkin, J.W. Elkins, E.M. Weinstock, B.W. Gandrud, G.C. Toon, M.R. Schoeberl, H. Jost, E.L. Atlas, T.P. Bui, J. Geophys. Res. **108** 8320 (2002). http://hdl.handle.net/2014/15631
8. M. Loewenstein, H. Jost, J. Grose, J. Eilers, D. Lynch, S. Jensen, J. Marmie, Spectrochim. Acta, Part A, Mol. Biomol. Spectrosc. **58**, 2329 (2002)
9. G. Durry, Spectrochim. Acta A **57**, 1855 (2001)
10. G. Moreau, C. Robert, V. Catoire, M. Chartier, C. Camy-Peyret, N. Huret, M. Pirre, L. Pomathiod, G. Chalumeau, Appl. Opt. **44**, 5972 (2005)
11. C.R. Webster, G.J. Flesch, D.C. Scott, J.E. Swanson, R.D. May, W.S. Woodward, C. Gmachl, F. Capasso, D.L. Sivco, J.N. Baillargeon, A.L. Hutchinson, A.Y. Cho, Appl. Opt. **40**, 321 (2001)
12. L.E. Christensen, C.R. Webster, R.Q. Yang, Appl. Opt. **46**, 1132 (2007)
13. G. Durry, I. Pouchet, N. Amarouche, T. Danguy, G. Megie, Appl. Opt. **39**, 5609 (2000)
14. L.S. Rothman, I.E. Gordon, A. Barbe, D. Chris Benner, P.F. Bernath, M. Birk, V. Boudon, L.R. Brown, A. Campargue, J.P. Champion, K. Chance, L.H. Coudert, V. Dana, V.M. Devi, S. Fally, J.M. Flaud, R.R. Gamache, A. Goldmanm, D. Jacquemart, I. Kleiner, N. Lacome, W.J. Lafferty, J.Y. Mandin, S.T. Massie, S.N. Mikhailenko, C.E. Miller, N. Moazzen-Ahmadi, O.V. Naumenko, A.V. Nikitin, J. Orphal, V.I. Perevalov, A. Perrin, A. Predoi-Cross, C.P. Rinsland, M. Rotger, M. Simeckova, M.A.H. Smith, K. Sung, S.A. Tashkun, J. Tennyson, R.A. Toth, A.C. Vandaele, J. Vander-Auwera, J. Quant. Spectrosc. Radiat. Transf. **110**, 533 (2009)
15. J. Fischer, R.R. Gamache, A. Goldman, L.S. Rothman, A. Perrin, J. Quant. Spectrosc. Radiat. Transf. **82**, 401 (2003)
16. S. Albert, S. Bauerecker, V. Boudon, L.R. Brown, J.P. Champion, M. Loëte, A. Nikitin, M. Quack, Chem. Phys. **356**, 131 (2009)
17. A.S. Pine, J. Quant. Spectrosc. Radiat. Transf. **57**, 157 (1997)
18. J.C. Hilico, J.P. Champion, S. Toumi, Vl.G. Tyuterev, S.A. Tashkun, J. Mol. Spectrosc. **168**, 455 (1994)
19. L.R. Brown, D. Chris Benner, J.P. Champion, V.M. Devi, L. Fejard, R.R. Gamache, T. Gabard, J.C. Hilico, B. Lavorel, M. Loete, G.Ch. Mellau, A. Nikitin, A.S. Pine, A. Predoi-Cross, C.P. Rinsland, O. Robert, R.L. Sams, M.A.H. Smith, S.A. Tashkun, Vl.G. Tyuterev, J. Quant. Spectrosc. Radiat. Transf. **82**, 219 (2003)
20. G. Durry, N. Amarouche, L. Joly, X. Liu, B. Parvitte, V. Zéninari, Appl. Phys. B, Lasers Opt. **90**, 573 (2008)
21. G. Durry, G. Megie, Appl. Optics **38** (1999)
22. D. Pieroni, Nguyen-Van-Thanh, C. Brodbeck, C. Claveau, A. Valentin, J.M. Hartmann, T. Gabard, J.P. Champion, D. Bermejo, J.L. Domenech, J. Chem. Phys. **110**, 7717 (1999)
23. D. Mondelain, S. Payan, W. Deng, C. Camy-Peret, D. Hurtmans, A.W. Mantz, J. Mol. Spectrosc. **244** (2007)